Simulations of M87 and Sgr A* imaging with the Millimetron Space Observatory on near-Earth orbits

Andrianov, A. S.; Baryshev, A. M.; Falcke, H.; Girin, I. A.; de Graauw, T.; Kostenko, V. I.; Kudriashov, V.; Ladygin, V. A.; Likhachev, S. F.; Roelofs, F.

Published in:
Monthly Notices of the Royal Astronomical Society

DOI:
10.1093/mnras/staa2709

Monthly Notices of the ROYAL ASTRONOMICAL SOCIETY
MNRAS **500,** 4866–4877 (2021) doi:10.1093/mnras/staa2709

Simulations of M87 and Sgr A∗ imaging with the *Millimetron* Space Observatory on near-Earth orbits

A. S. Andrianov,[1] A. M. Baryshev,[2] H. Falcke,[3] I. A. Girin,[1] T. de Graauw,[1] V. I. Kostenko,[1] V. Kudriashov,[3] V. A. Ladygin,[1] S. F. Likhachev,[1] F. Roelofs,[3] A. G. Rudnitskiy,[1]★ A. R. Shaykhutdinov,[1] Y. A. Shchekinov[1] and M. A. Shchurov[1]

[1]*Astro Space Center, Lebedev Physical Institute, Russian Academy of Sciences, Profsoyuznaya str. 84/32, Moscow 117997, Russia*
[2]*Kapteyn Astronomical Institute, University of Groningen, PO Box 800, 9700 AV Groningen, The Netherlands*
[3]*Research Institute for Mathematics, Astrophysics and Particle Physics (IMAPP), Radboud University, Heyendaalseweg 135, 6525 AJ Nijmegen, The Netherlands*

Accepted 2020 September 2. Received 2020 September 2; in original form 2020 June 18

ABSTRACT

High-resolution imaging of supermassive black hole shadows is a direct way to verify the theory of general relativity under extreme gravity conditions. Very Long Baseline Interferometry (VLBI) observations at millimetre/submillimetre wavelengths can provide such angular resolution for the supermassive black holes located in Sgr A∗ and M87. Recent VLBI observations of M87 with the Event Horizon Telescope (EHT) have shown such capabilities. The maximum obtainable spatial resolution of the EHT is limited by the Earth's diameter and atmospheric phase variations. In order to improve the image resolution, longer baselines are required. The *Radioastron* space mission successfully demonstrated the capabilities of space–Earth VLBI with baselines much longer than the Earth's diameter. *Millimetron* is the next space mission of the Russian Space Agency and will operate at millimetre wavelengths. The nominal orbit of the observatory will be located around the Lagrangian L2 point of the Sun–Earth system. In order to optimize the VLBI mode, we consider a possible second stage of the mission that could use a near-Earth high elliptical orbit (HEO). In this paper, a set of near-Earth orbits is used for synthetic space–Earth VLBI observations of Sgr A∗ and M87 in a joint *Millimetron* and EHT configuration. General relativistic magnetohydrodynamic models for the supermassive black hole environments of Sgr A∗ and M87 are used for static and dynamic imaging simulations at 230 GHz. A comparison preformed between ground and space–Earth baselines demonstrates that joint observations with *Millimetron* and EHT significantly improve the image resolution and allow the EHT + *Millimetron* to obtain snapshot images of Sgr A∗, probing the dynamics at fast time-scales.

Key words: instrumentation: high angular resolution – instrumentation: interferometers – quasars: supermassive black holes.

1 INTRODUCTION

Light from a luminous accretion disc around a black hole propagating at a distance within a few Schwarzschild radii forms a shadow with size $\sim 5r_S$ in the image plane (Bardeen 1973; Bardeen, Carter & Hawking 1973; Luminet 1979). The precise shape of the shadow depends on the black hole space–time geometry around the black hole and the distribution of emission from the accretion disc.

Currently, the best candidates for the study of the space–time geometry around a black hole are Sgr A∗ and M87. With a mass of $\sim 4.3 \times 10^6$ $M_\odot$ and a distance of ∼8.3 kpc (Ghez et al. 2008; Gillessen et al. 2009; Gravity Collaboration et al. 2018; Do et al. 2019a), the expected apparent size of the shadow of Sgr A∗ is about 53 μas. The supermassive black hole (SMBH) in M87 has a higher mass, of $\sim 3.5-6.6 \times 10^9$ $M_\odot$ (Gebhardt et al. 2011; Walsh et al. 2013; Event Horizon Telescope Collaboration et al. 2019a), but is located further away from the Earth at a distance of ∼17 Mpc (Bird et al. 2010). Consequently, the apparent size of the shadow of M87 is similar to that of Sgr A∗ and is about ∼40 μas.

Far-infrared (FIR) and submillimetre wavebands are optimal for imaging the shadow, because the ambient plasma is still transparent and refractive scattering decreases at these wavelengths (Falcke, Melia & Agol 2000; Mościbrodzka et al. 2009, 2014; Mościbrodzka, Falcke & Shiokawa 2016; Dexter, McKinney & Agol 2012).

Imaging the shadow is of great importance for testing the theory of general relativity (for recent discussions, see Psaltis 2019, Berti 2019, Cunha & Herdeiro 2018, and references therein). As has been shown by a number of authors (Bromley, Melia & Liu 2001; Broderick et al. 2009; Mościbrodzka et al. 2009; Dexter et al. 2010; Dexter et al. 2012; Kamruddin & Dexter 2013; Broderick et al. 2014), the feature most indicative of the presence of a shadow of a SMBH is an asymmetric photon ring, whose asymmetry encodes the most important parameters of the surrounding space–time metric: the SMBH mass, the spin, and its inclination relative to the observer's line of sight. The presence of a crescent-shaped structure around the horizon area in M87 was robustly confirmed by EHT in the 2017 campaign. It had a pronounced asymmetry – a clearly varying

★ E-mail: almax1024@gmail.com

thickness along the bright ring, and a deep (more than a factor of 10) brightness depression towards the centre (Event Horizon Telescope Collaboration et al. 2019b, f, a).

However, the main characteristic of the asymmetry – the mean difference between the outer and inner radius of the ring – is of the order of the gravitational radius (∼4 μas), and is too small to be resolved by the EHT (see Event Horizon Telescope Collaboration et al. 2019a). As discussed recently in Johnson, Lupsasca & Strominger (2019a), interferometry with longer baselines, 2 to 3 times the diameter of the Earth , is required for a detailed study of the space–time geometry and radiation transfer at the edge, having the same observational frequency of 230 GHz as it was in EHT ground VLBI observations. In addition to the limited EHT resolution, the effects of direct emission from the surrounding plasma make it difficult to accurately measure the photon ring with the current EHT array (Event Horizon Telescope Collaboration et al. 2019e, f; Johnson et al. 2019a).

A firm determination of the critical parameters of the supermassive black holes in Sgr A∗ and M87 will require a much higher angular resolution than can be obtained with ground-based interferometry. This can be achieved either with space–space VLBI, as described recently by Roelofs et al. (2019), or with space–Earth VLBI, which is possible within a joint program between the EHT and the *Millimetron* Space Observatory. In this paper, we describe synthetic observations of Sgr A and M87 with the joint EHT-*Millimetron* space–Earth VLBI. The paper is organized as follows. In Sections 1.1 and 1.2 we briefly review the EHT collaboration and the *Millimetron*. Section 2 describes the details of our simulations, including source models, *Millimetron* capabilities and orbit configurations. A description of synthetic observations, both averaged and dynamic, are given in Section 3, while Section 4 summarizes the results.

1.1 Event Horizon Telescope

The most recent effort to image a black hole shadow was made under the auspices of the EHT collaboration, a global ground millimetre VLBI array. The primary goal of the EHT is to observe the close environment of the SMBH Sagittarius A∗ (Sgr A∗) at the centre of our Galaxy and the SMBH in the centre of the giant elliptical galaxy M87 (Doeleman et al. 2009; Fish et al. 2013; Goddi et al. 2017).

Previous EHT measurements constrained the size of Sgr A∗ and M87 to 1.3 mm, but did not have sufficient (u, v) coverage to reconstruct an image of the source (Doeleman et al. 2008, 2012; Johnson et al. 2015; Lu et al. 2018). Phase closure measurements have indicated asymmetry in the structure of Sgr A∗ (Fish et al. 2016; Lu et al. 2018).

The first EHT imaging observations were conducted in 2017 April. These observations gave the first horizon-scale resolved image of M87. The mass of the supermassive black hole was measured, and the spin was constrained to be >0 by requiring the general relativistic magnetohydrodynamic (GRMHD) simulations in the EHT model space that reproduced the 1.3-mm structure to also produce a jet with enough power, as per observations on large scales (Event Horizon Telescope Collaboration et al. 2019b, c, d, a, f). The EHT opened a new era in physics and astronomy by enabling the direct study of space–time and physical processes at the edge of the event horizon of a black hole. At the same time, the rather restricted angular resolution (∼25 μas) achievable with ground-based VLBI does not look to be sufficient for a cogent solution of precise measurements of the asymmetry, mass and spin of a black hole. This difficulty calls for new observational technologies, such as space–Earth VLBI.

1.2 Millimetron mission

The most recent space-Earth VLBI was implemented via the *Radioastron* space mission, a 10-m space radio telescope that operated successfully for more than 7 years (Kardashev et al. 2013, 2015, 2017). *Radioastron* formed a space–Earth interferometer together with up to 60 ground telescopes at four frequencies: 0.3, 1.6, 4.8 and 22 GHz. It used an elliptical orbit with a minimal perigee of 400 km and a maximum apogee of ∼ 330 000 km (Kardashev et al. 2014a).

Observations with *Radioastron* showed that relatively compact active galactic nuclei (AGNs) are seen at 22 GHz with flux densities sufficient for detection even at baselines that correspond to an angular resolution of 11 μas, and the best sensitivity achieved at baselines for the *Radioastron*–Green Bank telescope at 1 cm was ∼10 mJy (Kovalev et al. 2020).

The *Millimetron* observatory will be a deployable 10-m, cooled, far-infrared, submillimetre and millimetre space telescope (Kardashev et al. 2014b). During the launch, the primary mirror and cryogenic screens will be folded in order to fit under the launcher fairing. In contrast to *Radioastron*, the *Millimetron* observatory will operate in two modes: single-dish and space–Earth interferometer.

In the single-dish mode, *Millimetron* will measure spectral distortions of the cosmic microwave background and magnetic fields, and observe filamentary structure and the water trail in the Galaxy. As part of the space–Earth interferometer, the goal of *Millimetron* is to provide high angular resolution for millimetre VLBI, which is crucial for studies of very compact astrophysical objects such as black holes. The space-Earth VLBI mode will be used to observe in a wide frequency range, from 33 up to 720 GHz (see Table 1).

The expected sensitivity of *Millimetron* (owing to the 125-times-wider bandwidth and higher effective antenna area) will be orders of magnitude greater than the sensitivity of *Radioastron*. This means that we can expect to detect a larger number of compact AGNs in VLBI mode, as well as the successful imaging of Sgr A∗ and M87.

The *Millimetron* space observatory will operate in a halo orbit around the L2 point of the Sun–Earth system. A halo orbit is a quasi-stable orbit, located in the vicinity of the L2 point in the plane perpendicular to the ecliptic plane. Such an orbital configuration is the most suitable for single-dish observations in terms of thermal and radiation conditions. The L2 orbit will provide the lowest possible temperature of the telescope mirror and thus allow it to reach maximum bolometric sensitivity.

For single-dish observations, the L2 orbit has another advantage – within half a year, *Millimetron* will be able to observe practically the full celestial sphere. However, for the VLBI mode, L2 orbits impose strict limitations on the space–Earth VLBI imaging observations. Feasibility studies of L2 orbits for space–Earth VLBI showed several significant disadvantages for imaging, as described below in Section 2.2 (Shaykhutdinov & Kostenko 2020). To resolve this, it is proposedthat the *Millimetron* observatory will operate also in high elliptical near-Earth orbit after the operation at the L2 point. Such a configuration allows better (u, v) coverage to be achieved for two-dimensional imaging observations. For the presented simulations, we selected two high elliptical orbits that have the possibility of transfer from the L2 halo orbit and are optimized for imaging Sgr A∗ and M87.

In contrast to *Radioastron*, *Millimetron* will perform space–Earth VLBI observations without simultaneous data transfer to the ground. The received signal will be digitized and stored in onboard memory (10 to 100 Tb, which corresponds to 1.5–15 h of observations). The

Table 1. Parameters of the *Millimetron* Space Observatory.

Parameter	Value
Primary mirror diameter	10 m
Primary mirror wavefront accuracy	< 10 μm rms
Primary mirror temperature	< 10 K at L2 orbit and ~ 70 K at elliptical orbit
Orbit	Anti-Sun Lagrangian L2 and High elliptical near-Earth orbit (HEO)
VLBI subsystem:	
VLBI Band 1 (to be confirmed)	33–50 GHz, $T_{sys} < 17$ K
VLBI Band 2	84–116 GHz, $T_{sys} < 37$ K
VLBI Band 3	211–275 GHz, $T_{sys} < 50$ K
VLBI Band 4 (to be confirmed)	602–720 GHz, $T_{sys} < 150$ K
Intermediate frequency bandwidth	1–2 GHz per 1 channel (up to 4 GHz)
Downlink data rate	1.2 Gbit s^{-1}
Time/frequency standard	Active hydrogen maser
Onboard memory	10–100 TB

Table 2. Parameters of ground telescopes at 230 GHz (Event Horizon Telescope Collaboration et al. 2019c). Telescope coordinates are represented in geocentric cartesian coordinate system (X, Y, Z) in meters. SEFD is a telescope sensitivity in Jy, D - telescope diameter in meters.

Telescope	X [m]	Y [m]	Z [m]	SEFD [Jy]	D [m]
Atacama Large Millimeter Array, Atacama, Chile (ALMA)	2225061.164	−5440057.37	−2481681.15	74	73
Atacama Pathfinder Experiment, Atacama, Chile (APEX)	2225039.53	−5441197.63	−2479303.36	4700	12
Greenland Telescope, Greenland (GLT)	1500692.00	−1191735.0	6066409.0	5000	12
IRAM 30-m millimeter radio telescope, Pico Veleta, Spain (PV)	5088967.900	−301681.6000	3825015.8000	1900	30
James Clerk Maxwell Telescope, Hawaii (JCMT)	−5464584.68	−2493001.17	2150653.98	10500	15
Large Millimeter Telescope, Mexico (LMT)	−768713.9637	−5988541.7982	2063275.9472	4500	50
Submillimeter Telescope, Arizona, United States (SMT)	−1828796.200	−5054406.800	3427865.200	17100	10
Submillimeter Array, Hawaii, (SMA)	−5464523.400	−2493147.080	2150611.750	6200	14.7
Kitt Peak National Observatory, Arizona, United States, (KP)[2020]	−1995678.840	−5037317.697	3357328.025	13000	12
Northern Extended Millimeter Array, Plateau de Bure, France (NOEMA)[2020]	4523998.40	468045.240	4460309.760	700	52

Note. [2020] telescopes to be added to the EHT in 2020.

Table 3. Orbit parameters.

Parameter	Type 1	Type 2
a	165 000 km	165 000 km
e	0.939	0.939
i	20.008°	323°
Ω	−3583°	170°
ω	−92°	−114°

Note. a, semimajor axis; e, orbit eccentricity; i, inclination; Ω, longitude of the ascending node; ω, argument of periapsis, i e. the orientation of the ellipse in the orbital plane. Period of both orbits is 10 days.

data transmission to ground can be performed after the observation or in the gaps between the observed scans. Such an approach will not limit the observations themselves. The expected mission launch date is 2029.

2 SIMULATIONS

2.1 Setup

The main goal of the simulations is to obtain (u, v) coverage for *Millimetron* space–Earth VLBI configurations and apply source models of Sgr A∗ and M87 to them. Such simulations illustrate the possible advantages of space–Earth VLBI.

The set of the simulations focuses on the high-resolution imaging of time-averaged models, neglecting the short-time variability of the sources. The second part focuses on observations of Sgr A∗ that are dynamic over time to study the variability of the brightness distribution around the shadow.

The following parameters were used in the simulations: the bandwidth $\Delta\nu = 2$ GHz, $t = 15$ h of total observing time at a central frequency of 230 GHz, to be compatible with the EHT. The total duration of observations t was selected according to the parameters of the *Millimetron* bandwidth $\Delta\nu$ and onboard memory capacity (100 Tb). The total volume of onboard memory is limited by mass constraints.

Simulations consist of several steps, as follows.

(i) Calculation of (u, v) coverages, taking into account the source visibility for space and ground telescopes.
(ii) Calculation of interferometric visibility functions for the corresponding (u, v) coverages using the specified source models.
(iii) Application of sensitivity, phase errors and noise.
(iv) Obtaining an initial dirty map.
(v) Image reconstruction.

Calculations of the (u, v) coverage and the model application, as well as the image reconstruction, were performed using Astro Space Locator Software (ASL). This software package is one of the results of the *Radioastron* mission development, which included establishing a data processing pipeline and software for post-correlation data analysis (Likhachev et al. 2017; Zuga, Rudnitskiy & Likhachev 2017). During the mission operations, this software was verified and used for fringe search, fringe fitting,

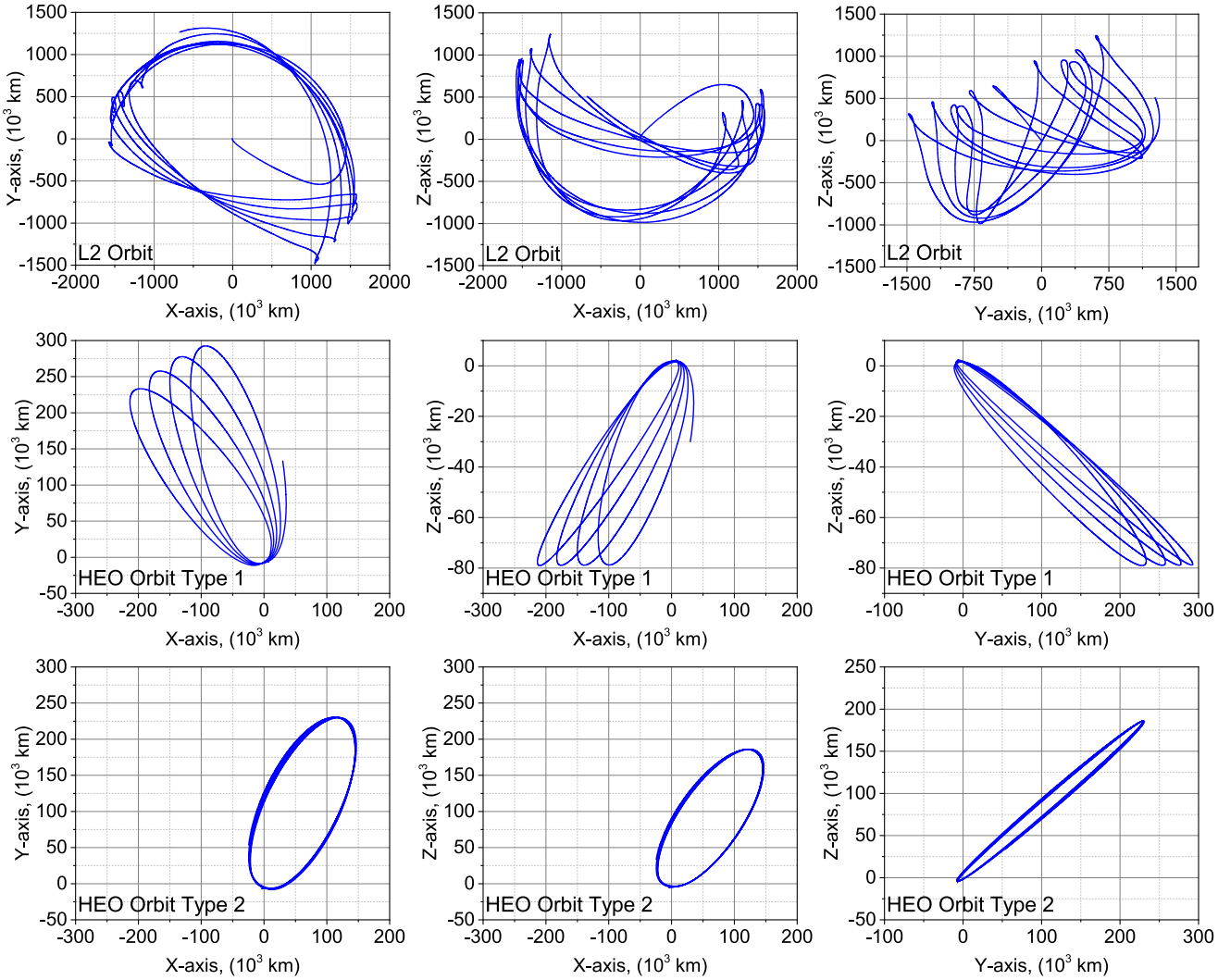

Figure 1. Projection of considered orbital configurations in the geocentric coordinate system. Top row: L2 orbit; middle row: HEO Orbit Type 1; bottom row: HEO Orbit Type 2. Coordinates are represented in thousands of kilometres.

imaging and simulations of VLBI observations. For ground support of space–Earth VLBI simulations, we used the telescopes of the EHT collaboration. The coordinates and parameters of all the telescopes used in our simulations are provided in Table 2.

Before proceeding with VLBI imaging simulations, we compared the performance of ASL with the EHT data processing pipeline, which uses maximum entropy method (MEM) imaging algorithms (Event Horizon Telescope Collaboration et al. (2019a), section 6.2.2). Furthermore, in order to identify the impact of the space–Earth baselines, we performed the simulations for pure ground baselines and space–Earth baselines.

Orbital calculations were performed with the software developed for *Millimetron* mission scheduling and flight dynamics calculations at the Astro Space Center of Lebedev Physical Institute.

We took the duration of a single observing segment according to the coherent integration time of 10 s. This value is a conservative estimate for the atmospheric coherence time at ground-based EHT sites. These limitations were taken into account in the sensitivity application step.

For Sgr A∗, we performed the simulations with the (u, v) coverage accumulated for 10 d, which corresponds to one orbital period; that is, 15 h or 5400 observing segments were distributed equally across the 10 d. For dynamic imaging, we calculated a set of (u, v) coverages, each corresponding to a single frame in the perigee of orbit.

For M87, we selected a 20-h region of the orbit, which covers baselines from 0.5 up to 6 Earth diameters. In this case, the total number of single observing segments was distributed across 20 h evenly as described above.

Owing to the fact that Sgr A∗ and M87 are located in different parts of the celestial sphere, a highly elliptical orbit with a given energy can be oriented in such a way as to provide the best (u, v) coverage over the entire period (about 9–10 d) for only one source. At the same time, such an orbit is capable of observing the second source with a baseline projection of less than 5 Earth diameters only in the perigee, that is, for ∼20 h.

The sensitivity for each baseline was calculated using the available ground telescope system equivalent flux density (*SEFD*) (see Table 2) (Chael et al. 2016, 2018; Event Horizon Telescope Collaboration et al. 2019c). For *Millimetron*, the estimated sensitivity (*SEFD*) at 230 GHz is ∼4000 Jy.

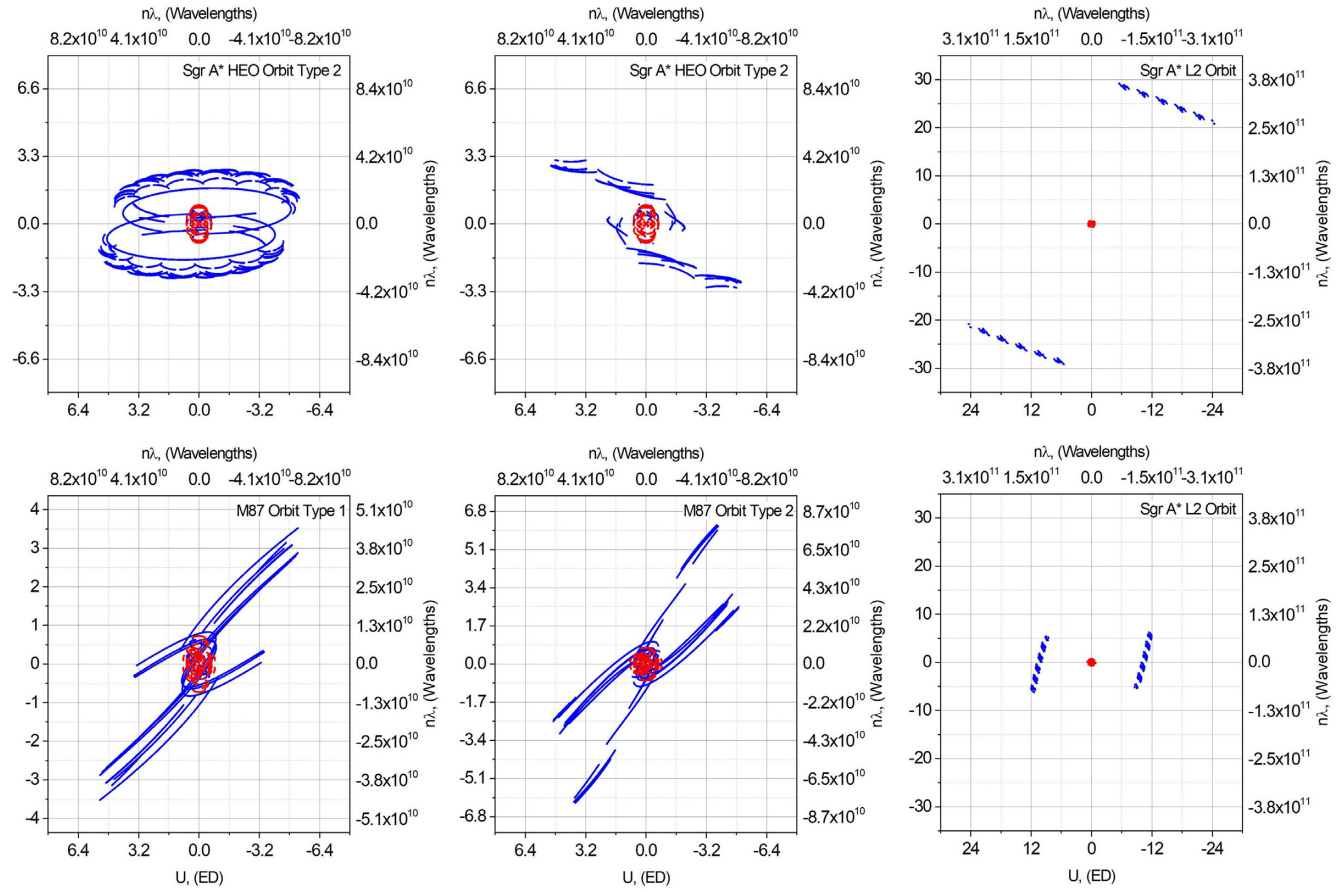

Figure 2. Top row: (u, v) coverage for Sgr A∗ (from left to right: Orbit Type 1, Orbit Type 2 and L2). Bottom row: (u, v) coverage for M87 (from left to right: Orbit Type 1, Orbit Type 2 and L2). Coordinates are represented in Earth diameters (bottom-X, left-Y axes) and wavelengths (top-X, right-Y axes). Red dots correspond to EHT ground baselines; blue dots correspond to EHT + *Millimetron* space–Earth baselines.

Simulations of baseline and telescope sensitivity in ASL were implemented as follows: a vector with an amplitude of sensitivity (calculated from the values of *SEFD*, bandwidth and integration time) and a random phase noise were added to each value of the visibility function in the resulting synthetically simulated observations.

For simplicity, the loss of absolute phase has not been considered in this paper. The simulations were performed using synthetic data and assume accurately calibrated phases on the ground–ground baselines. We believe that this error does not fundamentally affect image quality, because in this simulation we discuss *Millimetron* capabilities for a HEO orbit. Such an orbital configuration can generate enough closure phase triangles for imaging. While we neglect phase errors in this paper, in practice imaging should be done either with iterative CLEAN + self-calibration or directly with closure phases.

In order to perform a quantitative evaluation of image quality, we used the fidelity measure

$$F = \frac{MAX(M_i)}{\sqrt{\frac{1}{n}\sum_{i=1}^{n}(I_i - M_i)^2}}, \quad (1)$$

where F is the fidelity, M_i is the intensity at the ith pixel in the model image, I_i is the intensity at the ith pixel in the reconstructed image, and n is the number of pixels in the image.

2.2 Orbit configurations

A halo orbit around the L2 point of the Sun–Earth system provides the best environment for single-dish observations. At the same time, it lacks short- and intermediate-baseline projections for two-dimensional VLBI imaging. Shorter projections for space–Earth baselines provide fewer gaps in the (u, v) coverage and give intersections between the solely ground and space–Earth baselines. Having smaller gaps in the (u, v) coverage is crucial for the quality of the reconstructed image. Moreover, the period of the halo orbit is half a year, so for given sources short-baseline projections will be available only once per year for short time-spans (up to 2 d). This makes it difficult to obtain an acceptable (u, v) coverage and perform regular imaging VLBI observations with *Millimetron* at the L2 point.

For that reason, we considered the possibility of *Millimetron* operating in a near-Earth orbit. The choice fell on HEOs with apogee close to the Moon's orbit, because these types of orbits can provide transfer from L2 with gravity assist around the Moon (Kovalenko & Eismont 2018). Such a manoeuvre could save the Δv (momentum) budget for further mission stages.

For orbital calculations we used a Prince–Dormand propagator of the 5th order with adaptive step size (Dormand & Prince 1978), as it provides a good performance for HEOs. The force model included four harmonics of the EGM96 Earth gravity model (Lemoine et al. 1998) and perturbations from the Moon point mass. The ephemeris of the Moon was calculated using DE431 (Folkner et al. 2014).

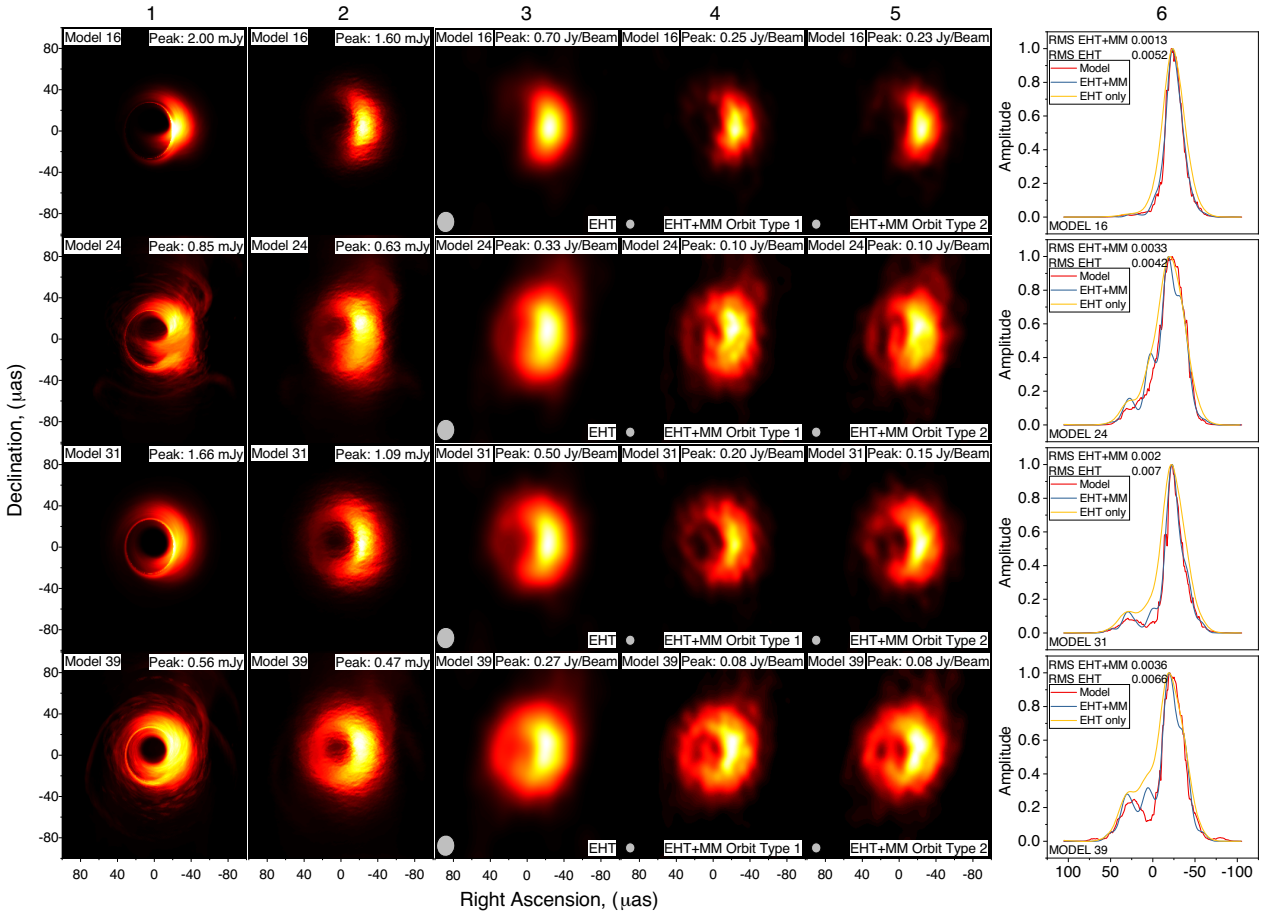

Figure 3. Results of simulations for Sgr A∗ static imaging at 230 GHz: initial models unscattered (column 1) and scattered (column 2), CLEAN images for EHT only (column 3), CLEAN images for *Millimetron* + EHT Orbit Type 1 (column 4), CLEAN images for *Millimetron* + EHT Orbit Type 2 (column 5). From top to bottom: model #16, model #24, model #31, model #39. Resulting image size: 200 × 200 μas. Column 6 depicts the brightness profiles as drawn from the origin (x, y) = (0, 0) along the positive direction of the x-axis; rms for EHT-only and *Millimetron* + EHT are shown in the left-uppermost corner of each plot. The size of the synthesized beam is 22 × 19 μas at –10°53 for the EHT-only configuration, and 10 × 10 μas at 9°84 for *Millimetron* + EHT. The colour scale is linear multiplied by the peak value of the corresponding panels.

The following orbital constraints were considered: distance at perigee $r_{\rm p} \geq$ 10 000 km, and distance at apogee $r_{\rm a} \geq$ 340 000 km. The goal was to obtain relatively compact (u, v) coverage within several Earth diameters (EDs).

The distribution of the points in the (u, v) plane depends on the semimajor axis, because it determines the lower limit of baseline projections. The upper boundaries for baseline projections were set as ≤5 ED, which corresponds to an angular resolution of ∼4 μas. Thus, the semiminor axis was set to $b = \sqrt{r_a r_p} \geq 56\,000$ km.

The calculations resulted in a set of orbits. Fig. 1 shows projections of the selected orbits represented in geocentric coordinate system. Among this set, two orbits were selected to have the minimal number of gaps in the (u, v) coverage for Sgr A∗ (Orbit Type 1; see Fig. 2, top) and for Sgr A∗ and M87 (Orbit Type 2; see Fig. 2 , bottom). The parameters of the selected orbits are shown in Table 3.

Orbit Type 2 in Table 3 was calculated to provide possible optimal imaging observations for two sources with acceptable (u, v) coverage. It was assumed that observations of M87 and Sgr A∗ will take place in different orbit sections. This orbit was used in the simulations for M87.

It is assumed that *Millimetron* will operate in a near-Earth orbit for at least several years. The range of tasks to be solved will not be limited to imaging of the two indicated sources, and it is planned to conduct observations of other compact extragalactic sources.

2.3 Source models

In our simulations we used the averaged models described in Mościbrodzka et al. (2014) for Sgr A∗ and kindly provided for us by M. Mościbrodzka. They include a set of time-averaged (over $\Delta t \approx$ 3 h) models: #16, #24, #31 and #39 in the nomenclature of Mościbrodzka et al. (2014, table 1), and are shown in Fig. 3 (left column). Models differ by the inclination angle i between the black hole spin and the observer's line of sight, the electron temperature $\Theta_{e,\rm j} = k_B T_e / m_e c^2$ in the jet, the ratio of proton to electron temperatures $T_{\rm p}/T_{\rm e}$, and the accretion rate $\dot{M}$ are shown in Table 4. The models have been chosen so as to emphasize their characteristic peculiarities, in order to better reveal the differences between imaging with EHT-only and EHT + *Millimetron*. Both diffractive and refractive scattering were included in the simulations for Sgr A∗ using the parameters constrained in Johnson et al. (2018).

It seems obvious, and is confirmed both in observations and in numerical simulations, that the flow of innermost accretion and

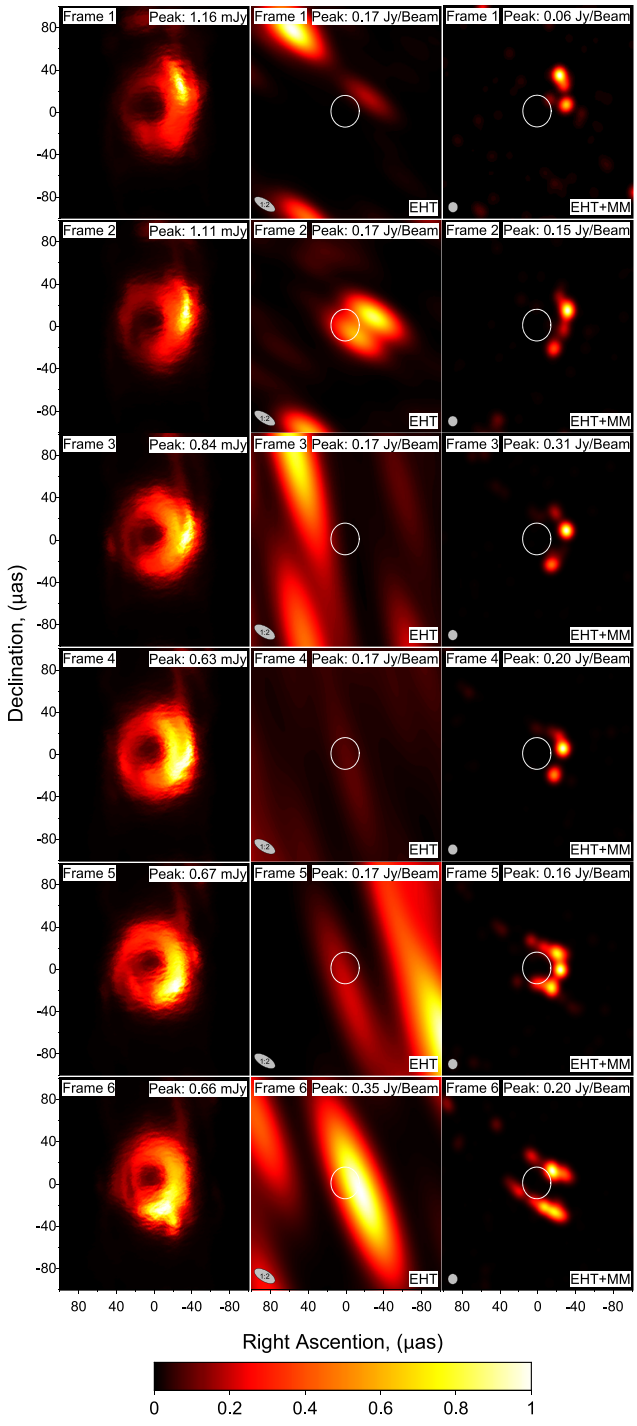

Figure 4. Dynamic simulations for Sgr A∗ (Orbit Type 1): snapshots of dynamic models (left); CLEAN images for the EHT-only configuration (middle); CLEAN images for *Millimetron* + EHT (right). Frames advance from top to bottom, with a time difference between the frames of 221 s. Resulting image size: 200 × 200 μas.The white circle in the centre of each image indicates the (0, 0) coordinates of the source. The colour scale is linear multiplied by the peak value of the corresponding panel.

its emissivity are time-dependent, and so their images around the shadow are as well. Near-infrared (NIR) monitoring of Sgr A∗ reveals variability on a wide range of time-scales from 20 s to hours, with variations of magnitude up to a factor of 10 (Witzel et al. 2018; Chen et al. 2019). In addition to such regular oscillations of disc emissivity, strong sporadic flares can also occur in the innermost region, such as, for example, the 'non-thermal bomb' in 2019 May detected in the NIR by the Keck Telescope (Do et al. 2019b) that occurred apparently within $\sim 10 r_g$ of the innermost accretion flow (Gutiérrez, Nemmen & Cafardo 2020). It is expected that such regular variability and explosive events might be manifested in the submillimetre range on similar time-scales. Therefore, dynamic interferometry is essential in order to understand the physical processes in this area, and also to monitor the effects of variability on the image itself. EHT + *Millimetron* capabilities are sufficient to perform observations of such variability with appropriate time resolution.

For dynamic simulations of Sgr A∗ we used model #39 (Fig. 4, left column) from Table 4. According to the modelling parameters, the time spacing between the GRMHD movie frames is 221 s. It is 10 times the gravitational time-scale of $t_g = GM/c^3$.

In our simulations of the ring around the shadow of M87, we used the model described by Johnson et al. (2019a). It is a time-averaged image of a GRMHD simulation of M87 with parameters chosen to be consistent with the EHT data of 2017 (Event Horizon Telescope Collaboration et al. 2019f) as specified in Johnson et al. (2019a). The parameters are as follows: $M = 6.2 \times 10^9 \mathrm{M}_\odot$, $a/M = 0.94$, $i = 163^\circ$, and the rate of mass accretion matches the flux density of EHT 2017 observations at 1.3 mm. Fig. 5 (a) shows the model.

3 RESULTS

3.1 Static images

Fig. 3 show CLEAN images of Sgr A∗ for EHT-only/*Millimetron* + EHT VLBI configurations.

The models of Sgr A∗ that were used in simulations (see Section 2.3) are averaged. These time-averaged images represent an idealized scenario for Sgr A∗, as GRHMD simulations predict a high time variability in the source. Of course, imaging the source will be much harder for Sgr A∗ when the underlying data is evolving in time. In this paper, we concentrate on the (u, v)-coverage quality anticipated for the HEO orbit. We assumed that after 10 d of integration, we will obtain a certain average image that will correspond well to the averaged GRMHD model. Fig. 6 shows the correspondence between the static image reconstruction of an averaged model (left panel) and the dynamic image reconstruction when the underlying data is evolving in time (right panel). From this figure it can be seen that the resulting images are quite similar, so we will use averaged models from now on. An additional reason for using the these models instead of the dynamic one is that the averaged model is better for fidelity computation, and simpler for comparison between model images and those obtainable with synthetic observations.

The quality of images obtained by EHT and EHT + *Millimetron*observations can be quantified by a characteristic similar to the sharpness of the inner edge defined in Event Horizon Telescope Collaboration et al. (2019a, see equations 22 and 23) as the ratio of the smoothing kernel width to the crescent diameter, $s = w_s/d_c$. The plots of normalized brightness profiles shown in the right panel of Fig. 3 illustrate differences in shadow sharpness obtained with EHT-only and with *Millimetron* + EHT VLBI. The differences between the model and EHT on the one hand and the model and EHT + Millimetron on the other can be seen from a comparison of the profiles along the x-axis for the model, EHT, and *Millimetron* + EHT are clearly smaller in the latter case. Their numerical values are given in Table 5. EHT + *Millimetron* synthetic observations show a factor

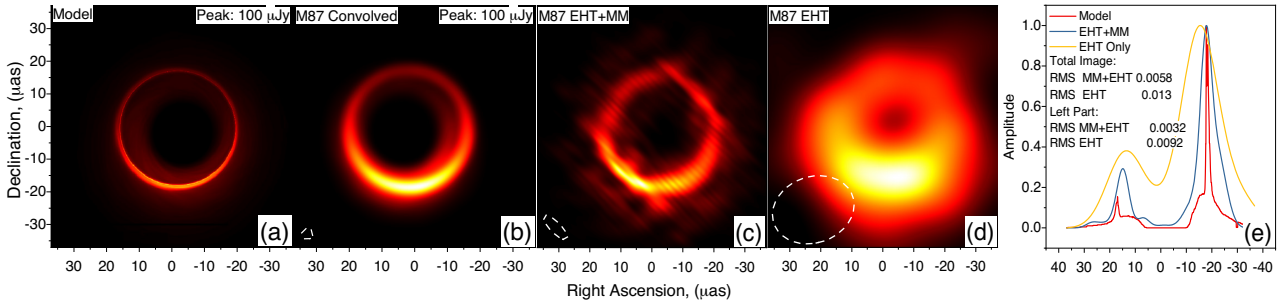

Figure 5. Results of simulations for M87 (Orbit Type 2) at 230 GHz: initial (a) and convolved (b) models, CLEAN images for *Millimetron* + EHT (c), CLEAN images for EHT only (d). Images size: 72 × 72 μas. White dashed lines show the synthesized beam; the size of the beam is 17.5 × 15.8 μas at –71°.56 for the EHT-only configuration and 5 × 5 μas at 46°.98 for *Millimetron* + EHT. The colour scale is linear multiplied by the peak value of the corresponding panels.

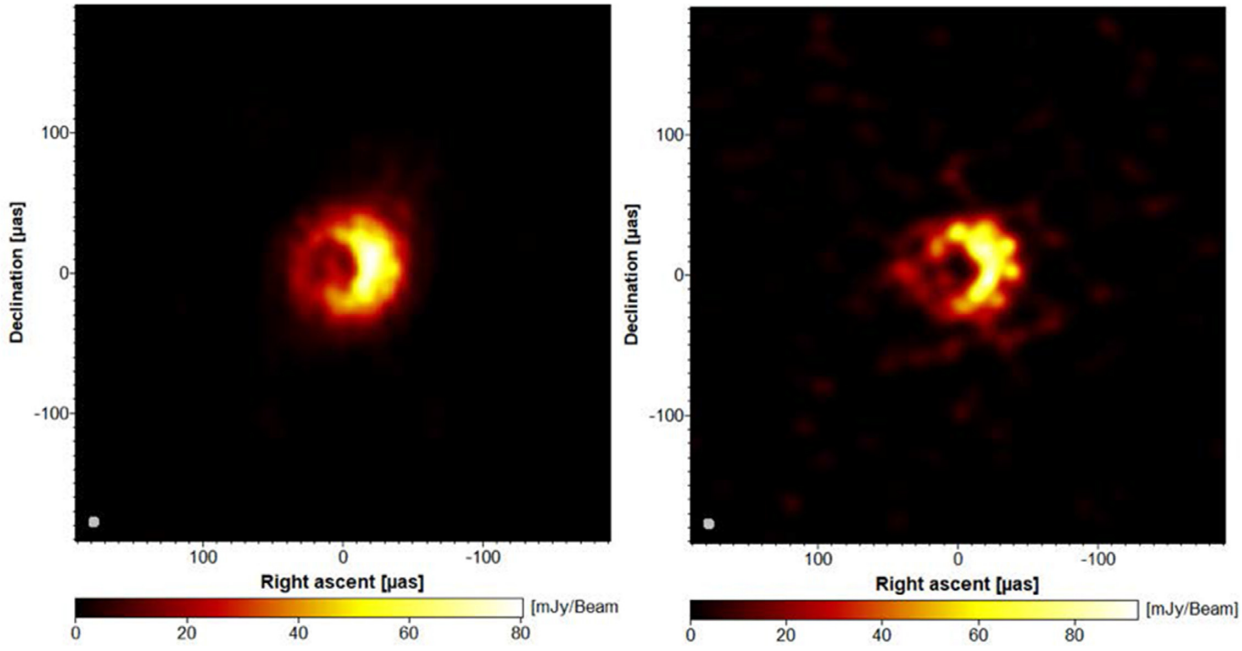

Figure 6. The left plot corresponds to imaging with Sgr A∗ model #39 (averaged model); the right plot corresponds to imaging with Sgr A∗ dynamic model #39 (80 different images merged together with time separation of 221 s).

of ∼2 better correspondence to the model sharpness. In addition, to avoid the effects of Doppler beaming at high inclination angles on to rms, we analysed the left part of the models separately and obtained image profiles (see Table 5, two last columns). EHT + *Millimetron* shows a better correspondence here as well, giving a more detailed imaging of fainter parts of the initial model.

Another characteristic is the flux depression, namely the ratio of the floor to the average over crescent brightness $f_{\rm d} = F_{\rm f}/\langle F_{\rm c}\rangle$, which can be roughly estimated from observations of brightness profiles in Fig. 3: brightness in the local minimum at the origin for *Millimetron* + EHT images is lower than for EHT-only ones, models 31 and 39 show the difference of about a factor of 2.

In order to characterize the quality of model image recovery, we use the normalized image fidelity and SSIM index (Wang et al. 2004). The normalized fidelity is given by (1), where both I_i and M_i images are normalized to 1. This represents synthesized image characteristics with respect to the original model in terms of the mean square difference. If images match perfectly, then the fidelity is infinite. The SSIM index correlates well with human perception of the image quality and is used here as a human-independent measure of this parameter (Wang et al. 2004). The SSIM index value ranges from 0 to 1. A SSIM index value of 1 is for two similar images. Table 6 shows fidelity for obtained images of Sgr A∗. For M87 we used the original model image as in Fig. 5(a) and a model image that is convolved with a circular Gaussian distribution of an angular size corresponding to the largest angular dimension of the synthesized beam for EHT + *Millimetron* image simulation, as in Fig. 5(b). The convolved image represents measurements of a model with an ideal diffraction-limited telescope with an aperture size of order of the *Millimetron* orbit. Comparison with this image allows us to analyse the relative amounts of image artefacts introduced as a result of a particular (u, v) coverage. Table 7 shows the fidelity and SSIM values for *Millimetron* + EHT and EHT-only images using the M87 model and the convolved M87 model as shown in Fig. 5(a)–(d). Both image quality measures demonstrate significant, up to 10 times, improvement of image reconstruction for *Millimetron* + EHT in comparison with EHT only. An especially clear difference is seen when a convolved image is used for comparison. It must be noted that *Millimetron* + EHT has a higher normalized fidelity than the

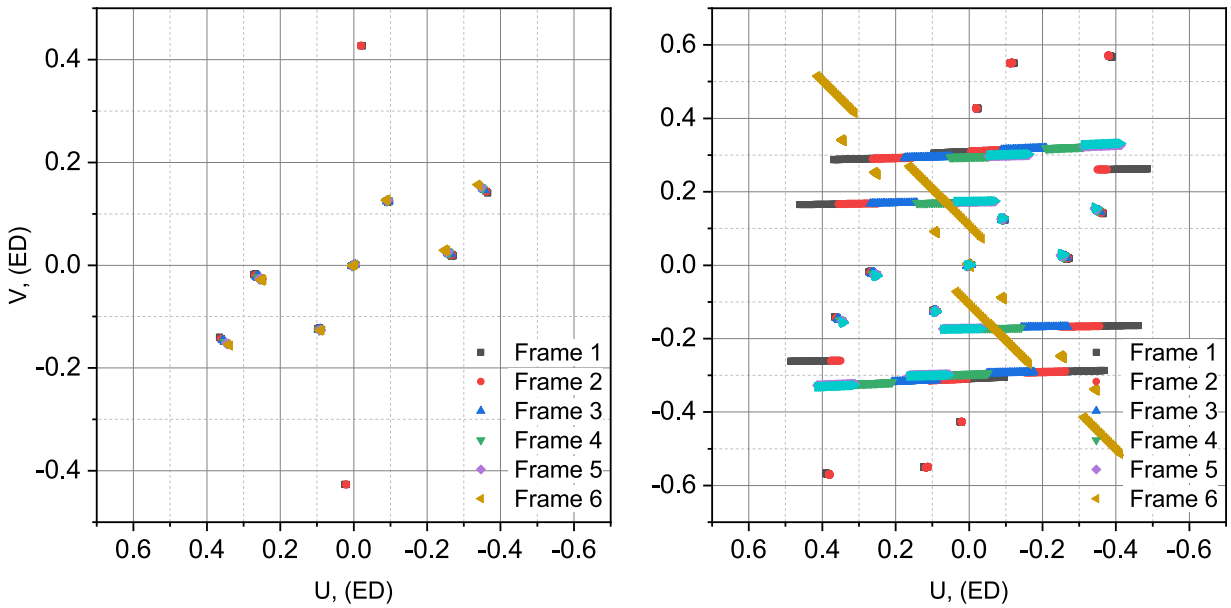

Figure 7. (u, v) coverage for Sgr A∗ dynamic simulations: EHT-only (left) and *Millimetron* + EHT (right, Orbit Type 1) dynamic frames. Coordinates are represented in Earth diameters. The total snapshot integration time is 1326 s (221 s per frame).

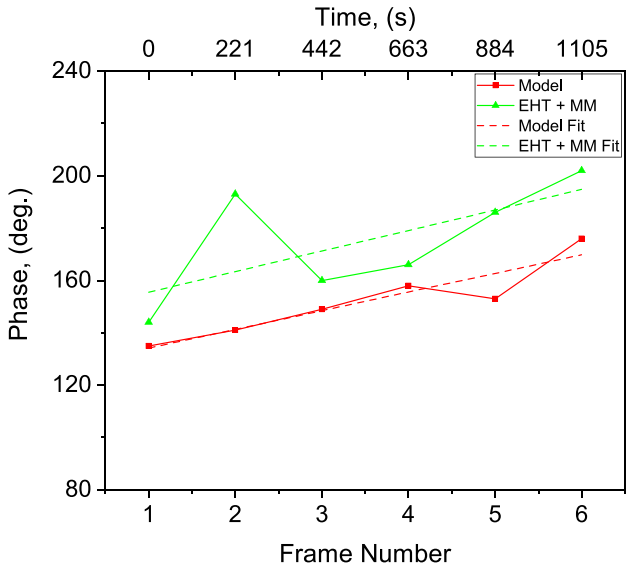

Figure 8. Estimation of asymmetry for dynamic imaging: the left panel shows the position of the centre of mass along phase φ of Sgr A∗ dynamic images. Solid lines corresponds to measured values, dashed lines correspond to a linear fit. .

convolved model, which reflects the fact that the convolution beam is a circular beam with an average size derived from the synthesized beam of *Millimetron* + EHT (u, v) coverage, which is elliptical. As a result, Fig. 5(c) contains more spatial information than Fig. 5(b).

Fig. 5 shows VLBI images of the photon ring model for M87 (the model is on Fig. 5) described by Johnson et al. (2019a), for EHT-only (middle) and *Millimetron* + EHT (right) synthetic observations.

The asymmetry of the images is related to the magnitude of the black hole spin and the angle between the axis of rotation of the black hole and the direction towards the observer. The positions of the centre of mass for the M87 source determined from Fig. 5 are presented in Table 8. The accuracy of the determination of the asymmetry parameter is higher for joint EHT and *Millimetron* observations.

Table 4. List of EHT models used for space–Earth VLBI simulations.

#	i	$\Theta_{e,\mathrm{j}}$	$(T_\mathrm{p}/T_\mathrm{e})_\mathrm{d}$	$\dot{M}$ [$\mathrm{M}_\odot\ \mathrm{yr}^{-1}$]
16	60°	10	5	3.9×10^{-9}
24	60°	20	20	4.2×10^{-8}
31	30°	10	5	5.6×10^{-9}
39	30°	20	20	4.1×10^{-8}

Notes. i is the inclination of the black hole spin to the observer's line of sight; $\Theta_{e,\mathrm{j}}$ is the electron temperature (in $m_e c^2$) in the jet; $(T_\mathrm{p}/T_\mathrm{e})_\mathrm{d}$ is the ratio of proton to electron temperature in the disc; $\dot{M}$ is the accretion rate. The nomenclature of models is as in Table in Mościbrodzka et al. (2014).

To estimate the degree of asymmetry of the images, we calculated the position of the centre of mass of each image:

$$X_\mathrm{cm} = \frac{\sum_{i=1}^{N} I_i\, x_i}{\sum_{i=1}^{N} I_i},$$

$$Y_\mathrm{cm} = \frac{\sum_{i=1}^{N} I_i\, y_i}{\sum_{i=1}^{N} I_i},$$

$$R_\mathrm{cm} = \sqrt{X_\mathrm{cm}^2 + Y_\mathrm{cm}^2},$$
$$\varphi_\mathrm{cm} = \arctan\left(Y_\mathrm{cm}/X_{cm}\right). \qquad (2)$$

Here, x_i, y_i are the coordinates of each image pixel, I_i is the intensity in the image pixel, and N is the number of image pixels.

It is more noticeable in the M87 example that introducing the space element to the VLBI configuration provides a higher resolution, leading to the finer structure observed in the images. The lack of scattering in the M87 galaxy clearly reveals the advantages of the space–Earth VLBI.

Table 5. Sharpness: rms for EHT only and *Millimetron* + EHT configurations.

#	EHT-Model	(EHT + *Millimetron*)-Model	EHT-Model	(EHT + *Millimetron* left side)-Model
16	0.0013	0.0052	0.0022	0.00069
24	0.0033	0.0042	0.0049	0.0045
31	0.002	0.007	0.0049	0.0019
39	0.0036	0.0068	0.0088	0.0052

Table 6. Fidelity of images obtained for Sgr A∗.

Sgr A∗ model	16	24	31	39
		Orbit Type 1		
Millimetron + EHT	61.39	49.49	54.18	41.2
EHT only	32.53	34.65	31.52	29.1
		Orbit Type 2		
Millimetron + EHT	59.58	45.77	52.14	37.97
EHT only	31.44	33.35	30.57	28.28

Table 7. Normalized fidelity and SSIM for images of M87.

Model	Convolved	*Millimetron* + EHT	EHT
		Normalized fidelity	
Model	9.79	12.56	2.25
Convolved	∞	22.40	2.55
		SSIM	
Model	0.286	0.345	0.012
Convolved	1	0.93	0.126

Table 8. Centre of mass position for M87 in polar coordinate system, where φ is the angular coordinate and ρ is the radial coordinate..

	Model	EHT only	*Millimetron* + EHT
φ	− 107.2	− 112.0	− 111.2
R	7.8	6.9	8.0

Table 9. Angular velocity of a bright-spot rotation in the Sgr A∗ dynamic model #39 (10^{-4} s^{-1}).

Dynamic Model #39	EHT only	*Millimetron* + EHT
5.6 ± 1.1	−1.0 ± 30.0	6.2 ± 3.5

3.2 Dynamic images of Sgr A∗

The second part of the simulations focused on dynamic imaging. The *Millimetron* spacecraft fly-by time for perigee of a HEO is about 20 min. In this portion of the orbit, the baseline projection changes within the interval 0.1–1 Earth diameters, resulting in fast (u, v) coverage evolution and providing the possibility of carrying out dynamical imaging of Sgr A∗.

According to the source model parameters, the time interval between the modelled movie frames for Sgr A∗ is 221 s, namely $\sim 10t_g$. Thus, we made an attempt to simulate short observations of the dynamic imaging in the HEO perigee.

Fig. 7 shows the (u, v) coverage for *Millimetron* + EHT (left) and EHT-only (right) dynamic simulation frames. Obviously, the (u, v) coverage of the ground-only VLBI configuration remains practically constant within such short time intervals, and dynamic imaging is not possible.

The resulting dynamic images for these simulations are represented in Fig. 4. The white circle in the centre of each image indicates the (0, 0) coordinates of the source. The time difference between the obtained images is 221 s. In other words, each single image corresponds to a given 221-s frame of the dynamic model.

The variations of brightness asymmetry around the shadow with characteristic time $t \sim 10t_g$ are clearly seen in Fig. 4 (left column), as is a varying flow in the contiguous parts of the disc. When averaged, these details merge into a heavily smeared image, as seen in Fig. 3 (left column).

We have estimated the position of the centre of mass for each frame of dynamic images of Sgr A∗. The results are presented in Fig. 8. For the *Millimetron* + EHT case, the position of the centre of mass coincides with the models, while for the EHT-only case, we have essentially random values.

Synthetic images are seen to turn their angular brightness distribution clockwise with time evolution, which may correspond to strong variations of brightness in the accretion disc comparable to the relativistic beaming around the shadow. This turn results in variations of the visible asymmetry, which can be distinguished by measurements of the instant brightness-weighed angle in the crescent. The estimated rotation velocity of this angle is given in Table 9.

From the slope of the fitted line in Fig. 8 (left), we estimated the angular velocity of bright-spot rotation in the Sgr A∗ model. The results are presented in Table 9. These results show that the quality of the reconstructed dynamic images from *Millimetron* + EHT is sufficient to determine the physical parameters from the image.

Regarding M87, the time variability for this source is ∼220 000 s, or $7t_g$: it is 1000 times higher than for Sgr A∗. Therefore, dynamic imaging observations at HEO perigee are not feasible for this source. Moreover, the shape of the orbit does not allow us to obtain a more or less stable (u, v) coverage for M87 in the dynamic observation mode. For these reasons, we do not present the results for M87 dynamic imaging for the HEO orbit. It is worth noting, however, that dynamic imaging of M87 in the perigee can reveal the time variation of local events at shorter time-scales $t \sim t_g$ near the shadow.

In future work, we plan to reconstruct dynamic images using different methods of dynamic imaging, as described in Johnson et al. (2017). This approach will reduce the impact of the side-lobes in the dirty beam on the resulting reconstructed image.

4 CONCLUSIONS

The goal of combined *Millimetron* + EHT space–Earth VLBI simulations was to demonstrate the capabilities of *Millimetron*, particularly when operating in a HEO. We calculated a set of high-elliptical near-Earth orbits for the *Millimetron* space observatory, which allow transition from the L2 point of the Sun–Earth system.

After that, we performed a feasibility study of these orbits using synthetic space–Earth VLBI observations of high-resolution imaging of the black hole shadow for M87 and Sgr A∗.

Not only do the results of these simulations show the capabilities of imaging in HEOs with *Millimetron*, but the HEOs provide a unique opportunity to observe Sgr A∗ dynamically. This means that if the space telescope has a sufficiently high velocity at perigee, and there are a sufficient number of ground-based telescopes and small baseline projections, one can obtain a rapidly evolving (u, v) coverage. This coverage allows us to reconstruct images with (u, v) sufficient for observing large-scale evolving structures ($\sim 60 t_g$) around the black hole dynamically.

Results of simulations for space–Earth VLBI imaging of a black hole with *Millimetron* have shown a significant improvement in spatial and temporal resolution over simulations with EHT only for the complex structures of modelled supermassive black hole sources. That is, a comparison of the reconstructed images obtained with EHT only and with the space–Earth interferometer EHT + *Millimetron* showed that the detailed structure of scattered models (the best examples demonstrated by models 24 and 39) is not resolved for the reconstructed images using the ground-only VLBI configuration. Note that the EHT ground array will likely be extended by the time *Millimetron* is operational, thus increasing the number of ground- and space–Earth baselines and improving the (u, v) coverage (Blackburn et al. 2019).

In addition, the resultant angular resolution and (u, v) coverages are evidently improved by *Millimetron*, as shown in the reconstructed images. The linear angular resolution for the simulated observations of M87 and Sgr A∗ for the EHT + *Millimetron* configuration is ∼6 times better than that for the ground-only configuration.

Finally, the main results of this paper clearly demonstrate the validated possibility of dynamic observations of Sgr A∗ with space–Earth VLBI baselines. Dynamic observations of the vicinity of a black hole are important for measuring the physical parameters of the black hole. Such observations have so far only been discussed for space–space VLBI configurations (Fish, Shea & Akiyama 2020; Palumbo et al. 2019; Roelofs et al. 2019).

ACKNOWLEDGEMENTS

The authors acknowledge M. Mościbrodzka for providing the GRMHD models for the described simulations. We would like to thank the reviewer for detailed analysis, valuable comments, remarks and criticism of this paper.

DATA AVAILABILITY

Data related to the results of simulations in this article will be shared on reasonable request to the corresponding author via e-mail.

REFERENCES

Bardeen J. M., 1973, in DeWitt C., DeWitt B. C., eds, Black Holes (Les Astres Occlus), Gordon & Breach, New York, p. 215
Bardeen J. M., Carter B., Hawking S. W., 1973, Comm. Math. Phys., 31, 161
Berti E., 2019, Gen. Relativ. Gravitation, 51, 140
Bird S., Harris W. E., Blakeslee J. P., Flynn C., 2010, A&A, 524, A71
Blackburn L. et al., 2019, BAAS, 51, 256
Broderick A. E., Fish V. L., Doeleman S. S., Loeb A., 2009, ApJ, 697, 45
Broderick A. E., Johannsen T., Loeb A., Psaltis D., 2014, ApJ, 784, 7
Bromley B. C., Melia F., Liu S., 2001, ApJ, 555, L83
Chael A. A., Johnson M. D., Narayan R., Doeleman S. S., Wardle J. F. C., Bouman K. L., 2016, ApJ, 829, 11
Chael A. A., Johnson M. D., Bouman K. L., Blackburn L. L., Akiyama K., Narayan R., 2018, ApJ, 857, 23
Chen Z. et al., 2019, ApJ, 882, L28
Cunha P. V. P., Herdeiro C. A. R., 2018, Gen. Relativ. Gravitation, 50, 42
Dexter J., Agol E., Fragile P. C., McKinney J. C., 2010, ApJ, 717, 1092
Dexter J., McKinney J. C., Agol E., 2012, MNRAS, 421, 1517
Do T. et al., 2019a, Science, 365, 664
Do T. et al., 2019b, ApJ, 882, L27
Doeleman S. et al., 2009, astro2010: The Astronomy and Astrophysics Decadal Survey, 2010, 68
Doeleman S. S. et al., 2008, Nature, 455, 78
Doeleman S. S. et al., 2012, Science, 338, 355
Dormand J. R., Prince P. J., 1978, Celest. Mech., 18, 223
Event Horizon Telescope Collaboration et al., 2019a, ApJ, 875, L6
Event Horizon Telescope Collaboration et al., 2019b, ApJ, 875, L1
Event Horizon Telescope Collaboration et al., 2019c, ApJ, 875, L2
Event Horizon Telescope Collaboration et al., 2019d, ApJ, 875, L3
Event Horizon Telescope Collaboration et al., 2019e, ApJ, 875, L4
Event Horizon Telescope Collaboration et al., 2019f, ApJ, 875, L5
Falcke H., Melia F., Agol E., 2000, ApJ, 528, L13
Fish V. et al., 2013, preprint (arXiv:1309.3519)
Fish V. L. et al., 2016, ApJ, 820, 90
Fish V. L., Shea M., Akiyama K., 2020, Adv. Space Res., 65, 821
Folkner W. M., Williams J. G., Boggs D. H., Park R. S., 2014, Interplanetary Network Progress Report, 196, 1–81
Gebhardt K., Adams J., Richstone D., Lauer T. R., Faber S. M., Gültekin K., Murphy J., Tremaine S., 2011, ApJ, 729, 119
Ghez A. M. et al., 2008, ApJ, 689, 1044
Gillessen S., Eisenhauer F., Trippe S., Alexander T., Genzel R., Martins F., Ott T., 2009, ApJ, 692, 1075
Goddi C. et al., 2017, Int. J. Modern Phys. D, 26, 1730001
Gravity Collaboration et al., 2018, A&A, 618, 15,
Gutiérrez E. M., Nemmen R., Cafardo F., 2020, ApJ, 891, L36
Johnson M. D. et al., 2015, Science, 350, 1242
Johnson M. D. et al., 2017, ApJ, 850, 172
Johnson M. D. et al., 2018, ApJ, 865, 104
Johnson M. D. et al., 2019a, Science Advances, 6, eaaz1310
Johnson M. D., Lupsasca A., Strominger A., 2019b, preprint (arXiv:1907.04329)
Kamruddin A. B., Dexter J., 2013, MNRAS, 434, 765
Kardashev N. S. et al., 2013, Astron. Rep., 57, 153
Kardashev N. S., Kreisman B. B., Pogodin A. V., Ponomarev Y. N., Filippova E. N., Sheikhet A. I., 2014a, Cosmic Res., 52, 332
Kardashev N. S. et al., 2014b, Phys. Uspekhi, 57, 1199
Kardashev N. S., Alakoz A. V., Kovalev Y. Y., Popov M. V., Sobolev A. M., Sokolovsky K. V., 2015, Sol. Syst. Res., 49, 573
Kardashev N. S. et al., 2017, Sol. Syst. Res., 51, 535
Kovalenko I. D., Eismont N. A., 2018, Astron. Lett., 44, 289
Kovalev Y. Y. et al., 2020, Adv. Space Res., 65, 705
Lemoine F. G. et al., 1998, NASA/TP-1998-206861, NASA Goddard Space Flight Center Technical Report, NASA, Goddard Space Flight Center, Greenbelt, Maryland
Likhachev S. F., Kostenko V. I., Girin I. A., Andrianov A. S., Rudnitskiy A. G., Zharov V. E., 2017, J. Astron. Instrum., 6, 1750004
Lu R.-S. et al., 2018, ApJ, 859, 60
Luminet J.-P., 1979, A&A, 75, 228
Mościbrodzka M., Gammie C. F., Dolence J. C., Shiokawa H., Leung P. K., 2009, ApJ, 706, 497
Mościbrodzka M., Falcke H., Shiokawa H., Gammie C. F., 2014, A&A, 570, A7

Mościbrodzka M., Falcke H., Shiokawa H., 2016, A&A, 586, A38
Palumbo D. C. M., Doeleman S. S., Johnson M. D., Bouman K. L., Chael A. A., 2019, ApJ, 881, 62
Psaltis D., 2019, Gen. Rel. Gravit., 51, 137
Roelofs F. et al., 2019, A&A, 625, A124
Shaykhutdinov A. R., Kostenko V. I., 2020, Space Res., 58, 394
Walsh J. et al., 2013, SnowPAC 2013 - Black Hole Fingerprints: Dynamics, Disruptions and Demographics. p. 6
Wang Z., Bovik A. C., Sheikh H. R., Simoncelli E. P., 2004, IEEE Trans. Image Processing, 13, 600
Witzel G. et al., 2018, ApJ, 863, 15
Zuga V. A., Rudnitskiy A. G., Likhachev S. F., 2017, Bull. Lebedev Phys. Inst., 44, 21

This paper has been typeset from a TEX/LATEX file prepared by the author.